Additively manufactured biodegradable porous magnesium

Li, Y.; Zhou, J.; Pavanram, P.; Leeflang, M. A.; Fockaert, L. I.; Pouran, B.; Tümer, N.; Schröder, K. U.; Mol, J. M.C.; Weinans, H.

Important note
To cite this publication, please use the final published version (if applicable).
Please check the document version above.

Full length article

Additively manufactured biodegradable porous magnesium

Y. Li [a,*], J. Zhou [a], P. Pavanram [b], M.A. Leeflang [a], L.I. Fockaert [c], B. Pouran [a,d], N. Tümer [a], K.-U. Schröder [e], J.M.C. Mol [c], H. Weinans [a,d,f], H. Jahr [b,g,1], A.A. Zadpoor [a,1]

[a] Department of Biomechanical Engineering, Delft University of Technology, Delft 2628CD, The Netherlands
[b] Department of Orthopaedics, University Hospital RWTH Aachen, Aachen 52074, Germany
[c] Department of Materials Science and Engineering, Delft University of Technology, Delft 2628 CD, The Netherlands
[d] Department of Orthopedics, UMC Utrecht, Heidelberglaan100, Utrecht 3584CX, The Netherlands
[e] Institute of Structural Mechanics and Lightweight Design, RWTH Aachen University, Aachen 52062, Germany
[f] Department of Rheumatology, University Medical Center Utrecht, Utrecht 3584CX, The Netherlands
[g] Department of Orthopedic Surgery, Maastricht UMC+, Maastricht 6202AZ, The Netherlands

ABSTRACT

An ideal bone substituting material should be bone-mimicking in terms of mechanical properties, present a precisely controlled and fully interconnected porous structure, and degrade in the human body to allow for full regeneration of large bony defects. However, simultaneously satisfying all these three requirements has so far been highly challenging. Here we present topologically ordered porous magnesium (WE43) scaffolds based on the diamond unit cell that were fabricated by selective laser melting (SLM) and satisfy all the requirements. We studied the *in vitro* biodegradation behavior (up to 4 weeks), mechanical properties and biocompatibility of the developed scaffolds. The mechanical properties of the AM porous WE43 ($E = 700–800$ MPa) scaffolds were found to fall into the range of the values reported for trabecular bone even after 4 weeks of biodegradation. Scanning electron microscopy (SEM), Fourier transform infrared spectroscopy (FTIR), electrochemical tests and μCT revealed a unique biodegradation mechanism that started with uniform corrosion, followed by localized corrosion, particularly in the center of the scaffolds. Biocompatibility tests performed up to 72 h showed level 0 cytotoxicity (according to ISO 10993-5 and -12), except for one time point (i.e., 24 h). Intimate contact between cells (MG-63) and the scaffolds was also observed in SEM images. The study shows for the first time that AM of porous Mg may provide distinct possibilities to adjust biodegradation profile through topological design and open up unprecedented opportunities to develop multifunctional bone substituting materials that mimic bone properties and enable full regeneration of critical-size load-bearing bony defects.

Statement of Significance

The ideal biomaterials for bone tissue regeneration should be bone-mimicking in terms of mechanical properties, present a fully interconnected porous structure, and exhibit a specific biodegradation behavior to enable *full* regeneration of bony defects. Recent advances in additive manufacturing have resulted in biomaterials that satisfy the first two requirements but simultaneously satisfying the third requirement has proven challenging so far. Here we present additively manufactured porous magnesium structures that have the potential to satisfy all above-mentioned requirements. Even after 4 weeks of biodegradation, the mechanical properties of the porous structures were found to be within those reported for native bone. Moreover, our comprehensive electrochemical, mechanical, topological, and biological study revealed a unique biodegradation behavior and the limited cytotoxicity of the developed biomaterials.

1. Introduction

Treatment of large bony defects is one of the major challenges in orthopedic surgery, as the current clinical solutions are still

associated with major limitations [1]. The quest for an ideal bone substituting material is therefore at its full swing [2]. Apart from being biocompatible, an ideal bone substitute should have mechanical properties close to those of bone to provide enough mechanical support and avoid stress shielding [3], present a fully-interconnected porous structure to allow for bone ingrowth [4,5], and degrade in the human body as the bone regenerates [6].

Recent advances in additive manufacturing (AM) techniques have enabled the fabrication of porous biomaterials satisfying the first two requirements, namely bone-mimicking mechanical properties [7] and fully interconnected porous structure with precisely controlled topological parameters [8]. AM bio-inert metallic materials such as titanium alloys [9–11], stainless steel [12], tantalum [13] and cobalt-chromium [14] combine a high level of interconnected porosity with bone-mimicking mechanical properties. However, they do not degrade over time, meaning that bone regeneration cannot be completed, while the surface of the implant may be colonized by bacteria that cause implant-associated infections [15]. Bio-inert implants may also cause long-term endothelial dysfunction, permanent physical irritation, and chronic inflammatory local reactions [16]. Biomaterials that satisfy all the three requirements including biodegradability are therefore of great benefit to the orthopaedic and traumatological community.

Magnesium and its alloys, as promising biodegradable metallic biomaterials, have been extensively investigated for potential orthopedic applications [17]. First, magnesium is an essential mineral for human nutrition and crucial to bone health [18]. Moreover, the mechanical properties of Mg alloys are close to those of bone [19]. Furthermore, Mg implants have been reported to stimulate new bone formation [19]. Therefore, Mg lends itself to the development of orthopedic implants [20]. However, as hydrogen released from the corrosion of Mg is problematic in many medical applications, the corrosion rate of Mg and its alloys should be carefully controlled [21]. One of the approaches to control the corrosion rate is adding alloying elements to Mg [22]. The addition of rare earth (RE) elements could improve both the mechanical strength and corrosion resistance [23–25]. Among Mg-RE alloys, WE43 has been considered suitable for orthopedic implant applications, based on pre-clinical and human trials in recent decades [26–28]. Up to now, several techniques to prepare magnesium scaffolds have been developed, including powder metallurgy with space holder, directional solidification, vacuum foaming, laser perforation, fiber deposition hot pressing and melt-extracted short fibers sintering [29–40]. It is, however, difficult (if not impossible) to use any of these methods to create fully interconnected porous structures, particularly when complex external shapes and intricate internal architectures in combination with adequate stiffness and strength are all required.

While AM techniques generally allow for the fabrication of complex and fully interconnected porous structures [41], their application to biodegradable metals in general and magnesium in particular has been very limited so far [42–44]. That is partially due to the fact that laser or electron beam processing of magnesium is technically extremely challenging. Magnesium is flammable even in its bulk form, let alone in the powder form that greatly increases the surface area and could cause dust explosion. Most laboratories therefore avoid AM of Mg out of safety concerns. Indeed, other than two abstracts [45,46], we are not aware of any previous reports on AM of porous Mg. Moreover, the biodegradation behavior of such scaffolds and the change in their mechanical properties along with biodegradation are not yet understood.

In this study, we applied SLM to build topographically ordered biodegradable WE43 scaffolds that have the potential to satisfy all the three above-mentioned requirements and conducted a full-scale study on their biodegradation behavior, biocompatibility,

the electrochemical aspects of their corrosion behavior, and the evolution of their mechanical properties during the degradation process.

2. Material and methods

2.1. Scaffold manufacturing and post processing

Diamond lattice (Fig. 1a) was adopted to design cylindrical porous specimens (Fig. 1b) with a diameter of 10 mm and a height of 11.2 mm. A strut size of 400 μm and a pore size of 600 μm were used, resulting in a relative density of 67% (design values). The specimens were then additively manufactured using a laboratory-scale SLM machine [46], in which argon was fed to maintain an inert atmosphere with oxygen content below 10 ppm. The optical system of the SLM machine consisted of a single-mode ytterbium fiber laser (IPG YLR-200) with a maximum output power of 230 W, a galvanometric scanner (SCANLAB hurrySCAN 20), and an f-theta focusing lens (SILL S4LFT 3254/126). The WE43 powder (4 wt% yttrium and 3 wt% rare earth elements) with a nearly spherical particle shape (Magnesium Elektron UK, Manchester, M27 8BF, UK) was gas atomized and sieved to a particle size range of 25–60 μm. After SLM, all samples were chemically polished for 2 min in a solution composed of 5% (in volume) HCl, 5% HNO_3, and 90% C_2H_5OH.

2.2. Microstructural characterization

Microstructures and compositions of WE43 specimens were examined using a scanning electron microscope (SEM, JSM-IT100, JEOL) equipped with an energy-disperse spectrometer (EDS). Phase identification was performed on the cross section using an X-ray diffractometer (XRD, Bruker D8 Advance diffractometer Bragg-Brentano geometry and Lynxeye position sensitive detector), operating at 40 kV and 40 mA with a step size of 0.034° and a dwell time of 2 s per step using Cu Ka radiation.

2.3. Immersion test

The rate of hydrogen gas evolution was determined eudiometrically in a custom-built set-up (Fig. 1c) placed in a thermal bath at 37 °C throughout the whole testing period of 28 days. Each sample was immersed inside a suspended 4-neck glass flask in the thermal bath with two micro pH meter electrodes (tip diameter: 3 mm, resolution: 45 μl, inLab NMR, METTLER TOLEDO) measuring pH values at the scaffold surface (i.e., local) and pH values further away (7 cm) from the sample (i.e., distant). The eudiometer connected to the flask had a volume of 400 ml with water as the confining liquid and was connected to a levelling bottle. The hydrogen produced in the flask supplanted the confining water in the eudiometer into the leveling bottle of 1000 ml. The gas volume was read when the leveling bottle was placed at the same level as the confining water in the eudiometer tube. For each reading, the temperature and air pressure were recorded in order to convert the measured gas volume to the gas volume in the standard state in accordance with DIN 38414-8. The following equation was used to calculate the standard gas volume values at different time points:

$$V_0 = V \cdot \frac{(P_l - P_w) \cdot T_0}{P_0 \cdot T}$$

V_0 – standard gas volume, ml
P_l – air pressure at the time of reading, mbar
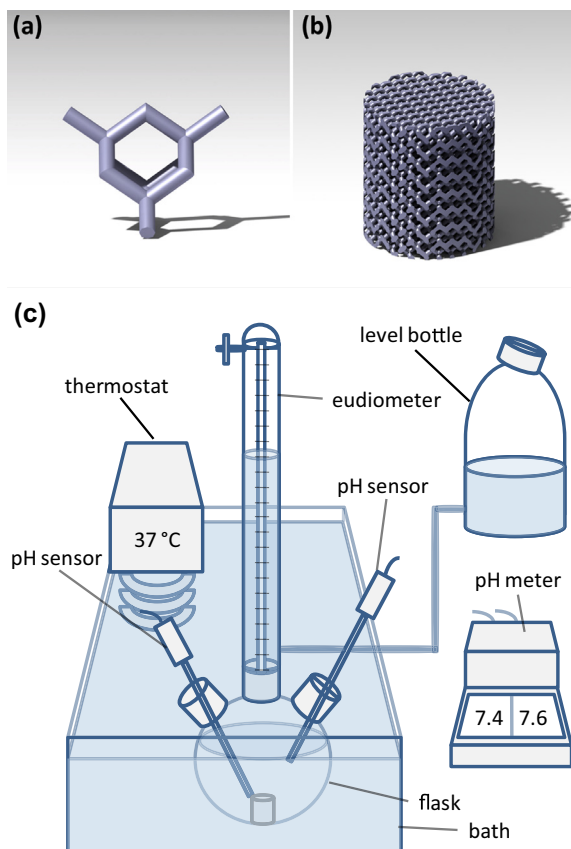
(a)

(b)

(c)

Fig. 1. Design of WE43 scaffolds and degradation study set-up: (a) diamond unit cell, (b) CAD model of the scaffold and (c) *in vitro* degradation eudiometer system.

P_w – vapor pressure of the water at the surrounding temperature, mbar

T_0 – standard temperature, K

P_0 – standard pressure, mbar

In total, 600 ml of revised simulated body fluid [47] (r-SBF) with 5% fetal bovine serum (FBS) was used for the tests, which were performed in triplicates. The medium was sampled after 1, 2, 7, 14, and 28 days of degradation and analyzed using an inductively coupled plasma optical emission spectroscope (ICP-OES, iCAP duo 6500 Thermo Fisher). Mg, Ca, and P ion concentrations in the solution were determined at different time points.

2.4. Characterization of degradation products

The morphology and composition at the surface of the specimens retrieved after the degradation tests were analyzed at selected time points by using the same SEM. In addition, Fourier-transform infrared spectroscopy (FTIR) spectra were obtained from a Thermo-Nicolet Nexus FTIR apparatus, equipped with a liquid-nitrogen cooled MCT-A (mercury-cadmium-telluride) detector and a SAGA grazing angle accessory at an incident angle of 80°. To collect absorption spectra, an infrared background was collected on a freshly polished sample prior to the analysis of the degraded samples, and the final spectra were compared against this background. For each spectrum, 128 scans at a resolution of 2 cm^{-1} were co-added.

2.5. Electrochemical tests

For electrochemical tests, specimens with an exposed surface area of 0.28 cm^2 to electrolyte were mounted in an epoxy resin

and ground with 800 grit SiC sandpaper. Copper screws were placed inside the resin to make these specimens conductive and electrochemical tests were performed in a 1250/1255 Solartron potentiostat in r-SBF with 5% FBS at 37 °C. A conventional three-electrode electrochemical cell was set up with platinum mesh as the counter electrode, Ag/AgCl as the reference electrode, and WE43 specimen as the working electrode. Open circuit potential (OCP) of the samples after immersion for different immersion periods up to 14 days was measured for 1 h. Potentiodynamic polarization (PDP) tests were then started at an initial potential of −0.3 V below OCP and was increased to +0.5 V above OCP at a scan rate of 0.5 mV/s.

2.6. Topological characterization

WE43 porous structures before and after immersion were imaged by μCT (Quantum FX, Perkin Elmer, USA) with a tube current of 180 μA and a tube voltage of 90 kV, a scan time of 3 min, and a resolution of 30 μm. μCT images were automatically reconstructed and converted into a series of 2D images using Analyze 11.0 (Perkin Elmer, USA). Then the images were exported to Fiji (NIH, Bethesda, MD, USA) and regions of interest (ROIs) were defined. Two different thresholds (80 and 119) were applied to segment samples with the lower value incorporating most of the degradation products and the higher value segmenting the degradation products apart from the Mg alloy. After segmentation in Fiji, the ratio of the void volume to the 3D ROI volume, strut size, and pore size were calculated by the prebuilt plugin of BoneJ (available in ImageJ). In addition to μCT, SEM and back-scattered electron imaging (BSE) were applied to observe the cross section of the degraded scaffolds at low magnifications.

2.7. Mechanical characterization

Compression tests were carried out using an Instron machine (10 kN load cell) at a crosshead speed of 2 mm/min. The mechanical properties of the porous structures were determined according to ISO 13314:2011. For the as-built, as-polished, and as-degraded specimens, the quasi-elastic gradient (hereafter referred to as Young's modulus) and yield strength were obtained. The slope of the initial linear part of the stress-strain curve was measured to determine the Young's modulus of the porous structures. The initial linear part of the stress-strain curve was offset by 0.2% and its intersection with the stress-strain curve was taken to calculate the yield strength. The stress-strain curves were measured at different immersion time points (i.e., 1, 2, 7, 14 and 28 days). The tests were performed in triplicates per time point and the average values of Young's modulus and yield strength were calculated.

2.8. Cell culture assays

Human osteoblast-like cell line MG-63 (ATCC, CRL-1427) was cultured in Dulbecco's modified eagle medium (DMEM, Sigma-Aldrich) with 10% FBS (PAN-Biotech GmbH, Aidenbach, Germany) at 37 °C, 5% CO$_2$ and 95% humidity. After immersion in 2-propanol (Merck, Darmstadt, Germany) for 30 min, specimens were weighed and incubated in DMEM (Sigma-Aldrich) with 10% FBS (PAN-Biotech GmbH, Aidenbach, Germany) under physiological conditions (5% CO$_2$, 95% humidity and 37 °C) according to the recommendation of Wang et al. [48]. Extracts were prepared according to EN ISO standards 10993-12 using a mass-to-volume ratio for irregularly shaped devices as the ratio of sample mass to extractant volume. For WE43, we used the ISO 10993 standard of 0.2 g/mL of medium with the recently recommended modification of ISO10993-12 for biodegradable magnesium-based materials by Wang et al. [48]: 10-times diluted extracts of five randomly chosen

WE43 scaffolds from the same production batch were used for assessing *in vitro* cytotoxicity. As per ISO 10993-12, specifically acceptable extraction condition, we used 37 °C for 72 h under static condition. Our earlier reported biocompatible SLM-built titanium (Ti-6Al-4V) specimens of similar design [49] served as reference material (positive control) (extraction ratio 0.2 g/ml) and sulforaphane (10 μM), for which cytotoxic effects were reported for MG-63 cells [50], was used as negative control.

In a 96 well plate, 2500 MG-63 cells were seeded per well and pre-cultivated for 12 h as described above, prior to exchanging the culture medium with WE43 extracts. Cells were then incubated for 0, 24, 48 and 72 h under the same cell culture conditions. The cytoxicity of WE43 extracts was evaluated using the MTS assay (Promega, CellTiter 96® AQueous One Solution Cell Proliferation Assay G3580) according to the supplier's instructions. Briefly, prior to adding MTS tetrazolium compound, control media and WE43 extracts were replaced with fresh cell culture medium in order to prevent any interference of the magnesium extract with the tetrazolium salt [51]. At the indicated time points, 20 μl of CellTiter 96® AQueous One Solution Reagent was added per well, containing MG-63 indicator cells in 100 μl of culture medium, prior to incubation at 37 °C for 2 h. Absorbance was recorded at 490 nm using a 96-well plate reader.

For the live-dead assay, WE43 and Ti-6Al-4V specimens were incubated for 48 h with DMEM + 10% FBS, as described above. After incubation, the specimens were carefully, dropwise seeded with 75,000 MG-63 cells per mm height in fresh cell culture medium and incubated for 1 h under cell culture conditions, prior to adding 2 ml of fresh medium. After 24 h of incubation, live and dead dye (Live and Dead Cell Assay kit, Abcam, ab115347) was applied to the specimens according to the supplier's instructions and incubated for 10 min at room temperature. Cell seeded scaffolds were analyzed using fluorescent microscopy (LIVE: Emission (max): 495 nm, Excitation (max): 515 nm and DEAD: Emission (max): 528 nm).

SEM analysis of the cell-seeded specimens was performed as previously described [52]. Briefly, cell-seeded scaffolds were carefully rinsed in phosphate buffered saline and fixed for 1 h in 3% glutaraldehyde (Agar scientific, Wetzlar, Germany) in 0.1 M Soerensen's phosphate buffer (Merck, Darmstadt, Germany) at room temperature followed by 10 min dehydratation steps in 30, 50, 70, 90 and 100% ethanol (last step twice). The samples were then air-dried at room temperature prior to sputter-coating (Sputter Coater EM SCD500, Leica, Wetzlar, Germany) with 12.5 nm of gold-palladium and imaged at 10 kV in SEM (ESEM XL 30 FEG, FEI, Eindhoven, Netherlands).

2.9. Statistical analysis

Optical density data (MTS) were normalized to the lysis buffer and unconditioned culture medium controls. Cytotoxicity was then analyzed by two-way ANOVA and post-hoc Tukey's multiple comparisons test ($\alpha = 0.05$) with $p < .0001$, ****; $p < .001$, ***; $p < .01$, **; $p < .05$, *; *n.s.* = not significant.

3. Results

3.1. Surface morphology and microstructure of the scaffolds

Unmelted powder particles were present on the surface of the as-built specimens (Fig. 2a). After chemical polishing, the surface of the specimens on the periphery became relatively smooth (Fig. 2a), while the roughness of struts in the center was still high. Flake-shaped, homogeneously distributed white second-phase particles were found on the surface of the as-polished specimens

(Fig. 2a). The stacking of the melt pools in the build direction could be observed in all struts (Fig. 2b). Two different microstructural features were observed in the as-built specimens. At the bottom of the struts, the microstructure was dominated by rose-like fine grains with grain sizes around 5 μm (Fig. 2c). At the top of the struts, however, the microstructure was featured by cellular morphology with a width of <1 μm (Fig. 2d). White flake-shaped second-phase particles were present throughout the magnesium matrix. EDS analysis showed that these white particles (Fig. 2e, spot 002) contained a higher concentration of yttrium than the magnesium matrix (Fig. 2e, spot 001). XRD revealed the presence of Y_2O_3 and Mg_3Nd in the as-built material (Fig. 2f), suggesting that the white particles could be yttrium oxide.

3.2. In vitro degradation behavior of the scaffolds

White degradation products gradually formed on the surface of the struts along with increasing immersion time (Fig. 3a). At day 28, the scaffolds still maintained their structural integrity without obvious detachment of degraded particles.

Hydrogen gas evolution increased rapidly at the early time points, but slowed down gradually after day 1 (Fig. 3b). However, at some time intervals (e.g., 4–6 days), the slope of the hydrogen release curve increased again. Until day 28, Mg ion concentration increased from 37.5 to 145.7 mg/L (Fig. 3c) with a substantial increase between days 2 and 7. Over this period, Ca and P ion concentrations decreased. The pH changes were very different in the proximity of the scaffold and further away (Fig. 3d, e). During the first 3 h, the local pH increased from 7.4 to 8.1 and decreased gradually thereafter, while the distant pH was still within the biological (neutral) range of pH 7.4–7.5 (Fig. 3d). For longer immersion times, the local pH values were always slightly higher than the distant pH values (Fig. 3e).

3.3. Characterization of degradation products on the scaffolds

The surfaces of the degraded specimens contained cracks and were covered by a deposition layer (Fig. 4a). After 1 day, small white degradation products formed on the surface close to the flake-shaped particles (Fig. 4a, spot 001). The degradation products contained Mg, C, O, and Y (Fig. 4b, spot 001) and were most likely hydroxides and carbonates. At day 2, the white degradation products became larger, but with the elemental composition similar to day 1 (Fig. 4b, spot 002). At day 7, some needle-shaped crystals formed on the surface of the former layer and P was detected for the first time (Fig. 4b, spot 003). After 14 days, apart from carbonates, rod-like products appeared on the surface, which contained Ca and P (Fig. 4b, spot 004). After 28 days, a compact layer formed with a Ca/P ratio around 1.5 (Fig. 4b, spot 005). FTIR spectra further revealed the presence of phosphates and carbonates in the corrosion layer (Fig. 4c) with characteristic phosphate-specific absorption bands at about 1200 and 940 cm^{-1}, respectively, corresponding to the v3 and v1 vibrational modes [53], while the peaks at 1740 cm^{-1} likely resulted from CO_3^{2-} [54]. Carbonate absorption peaks emerged during the first day of the immersion tests (Fig. 4c) and increased onwards, which was accompanied by the appearance of the peaks of phosphates from day 2 (Fig. 4c), suggesting the formation of an apatite-like corrosion layer.

3.4. Electrochemical behaviors

Polarization curves of specimens at different immersion time points (Fig. 5a) showed a passivation stage in the anodic polarization branch for all the samples. Noble shift of OCP was observed from 1 h to 5 h, while the potential began to decrease from day 1 to day 2 and increased again after day 7 (Fig. 5b). Corrosion current
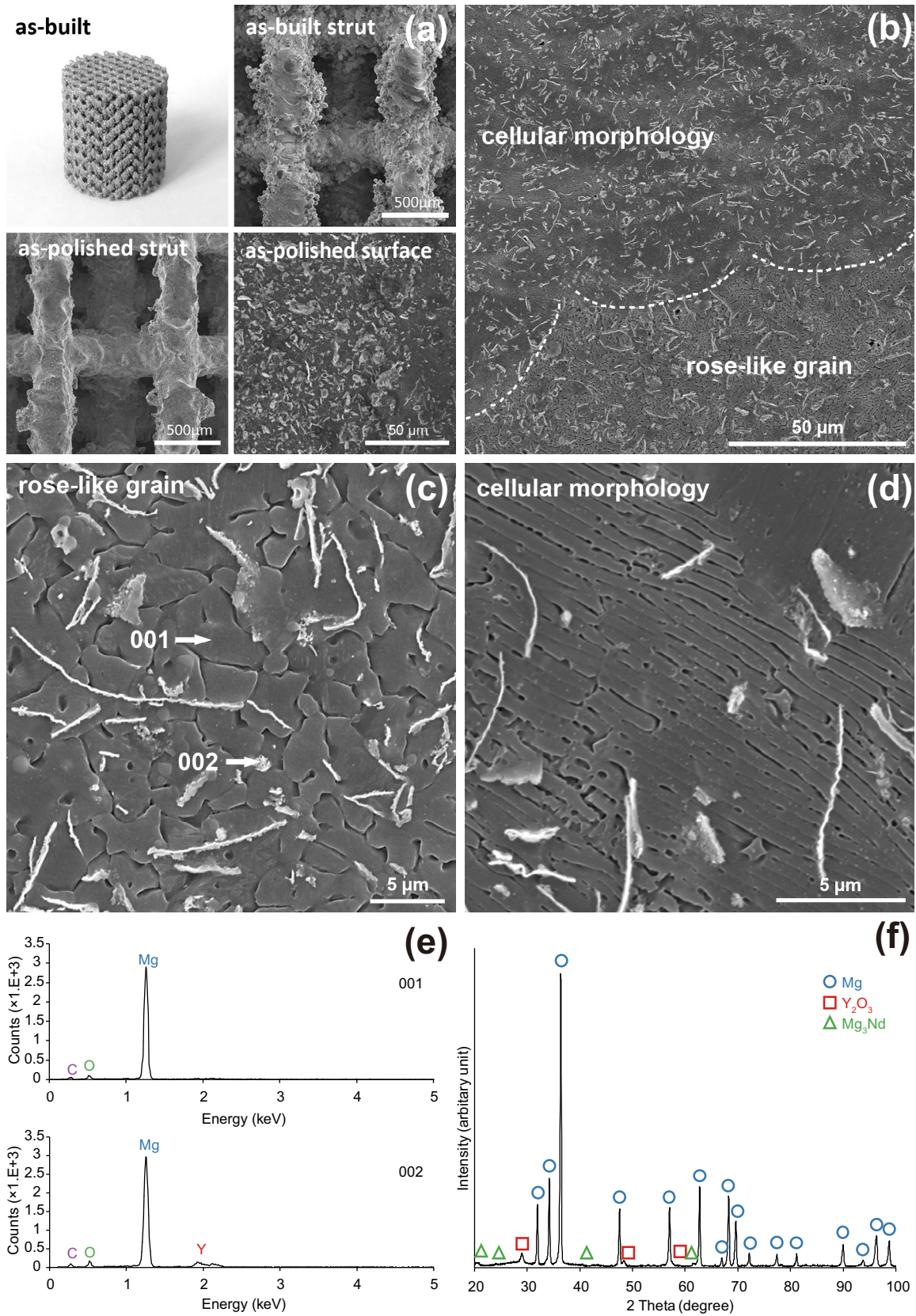
Fig. 2. Surface morphology, microstructure and composition analyses: (a) surface morphology on the periphery of scaffolds, (b) SEM image of melt pool, (c) (d) SEM images of rose-like grains and cellular morphology at higher magnification, (e) EDS analysis and (f) XRD analysis.

density i_{corr} values were calculated by using the cathodic Tafel extrapolation considering the non-symmetrical polarization curves between the anodic and cathodic branches. The current density increased from $3.1 \cdot 10^{-5}$ to $6.1 \cdot 10^{-5}$ A·cm^{-2} during 24 h and began to fall after 24 h, decreasing to $2.1 \cdot 10^{-5}$ A·cm^{-2} by day 14 (Fig. 5b).

3.5. Topological characterization

The as-built scaffolds were measured (threshold 2) to have an average strut size of $420 \pm 4\,\mu m$ (design value $= 400\,\mu m$) and porosity of $64\% \pm 0.2\%$ (design value $= 67\%$) (Fig. 6a, c).

When both WE43 and degradation products were segmented with the lower threshold of 80, the strut size slightly increased after 1 day and 2 days, reaching the maximum value at day 7 followed by continuous decrease till day 28 (Fig. 6a). Similarly, the pore size decreased continuously until day 14 and then increased at day 28 (Fig. 6b).

Segmenting the scaffold material at the higher threshold of 119 (thus removing the corroded material), however, showed that the strut size decreased with increasing immersion time, and subsequently a slight increase at day 28 (Fig. 6a). The pore size showed only slight changes till day 2, while increasing from day 7 to day 28 (Fig. 6b). During 28 days, scaffolds lost 20.7% of their volume (Fig. 6c), which was comparable with amass reduction of 19.2% calculated from hydrogen release. The changes in porosity were similar to those of pore size regardless of the segmentation threshold (Fig. 6d).

There were differences between threshold 1 and threshold 2 segmentations even for the as-built specimens, meaning that these two thresholds could not perfectly separate the scaffold material from degradation products, as there was some overlap between the attenuation coefficients of both materials. Nevertheless, the general (qualitative) trends reported here remain valid.

Reconstructed μCT images (green = WE43, blue = degradation products) showed significant formation of degradation products at the center of the scaffolds, while only limited quantities of degradation products were formed at the outer layers of the specimens (Fig. 6e). SEM images particularly in the BSE mode confirmed the μCT results, showing that WE43 (white) was replaced by more degradation products (gray) at the center of the scaffolds than that at the periphery (Fig. 7a, b).

3.6. Mechanical properties

Under compression, the as-built and as-polished scaffolds exhibited the typical stress-strain behavior of porous structures
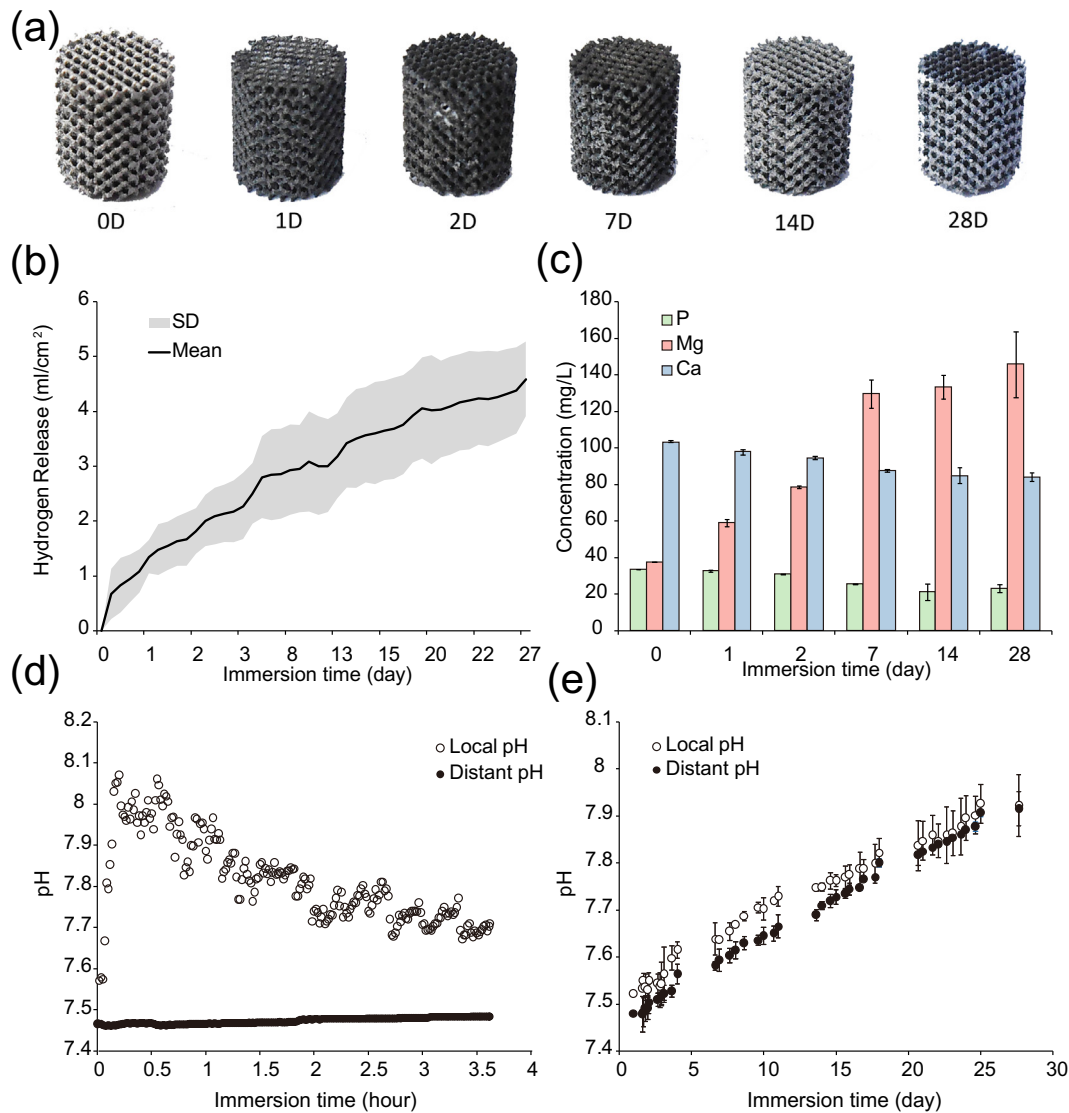

Fig. 3. *In vitro* degradation tests: (a) visual evaluation of as-degraded samples, (b) hydrogen release, (c) ion release, (d) short term pH variation and (e) long term pH variation.
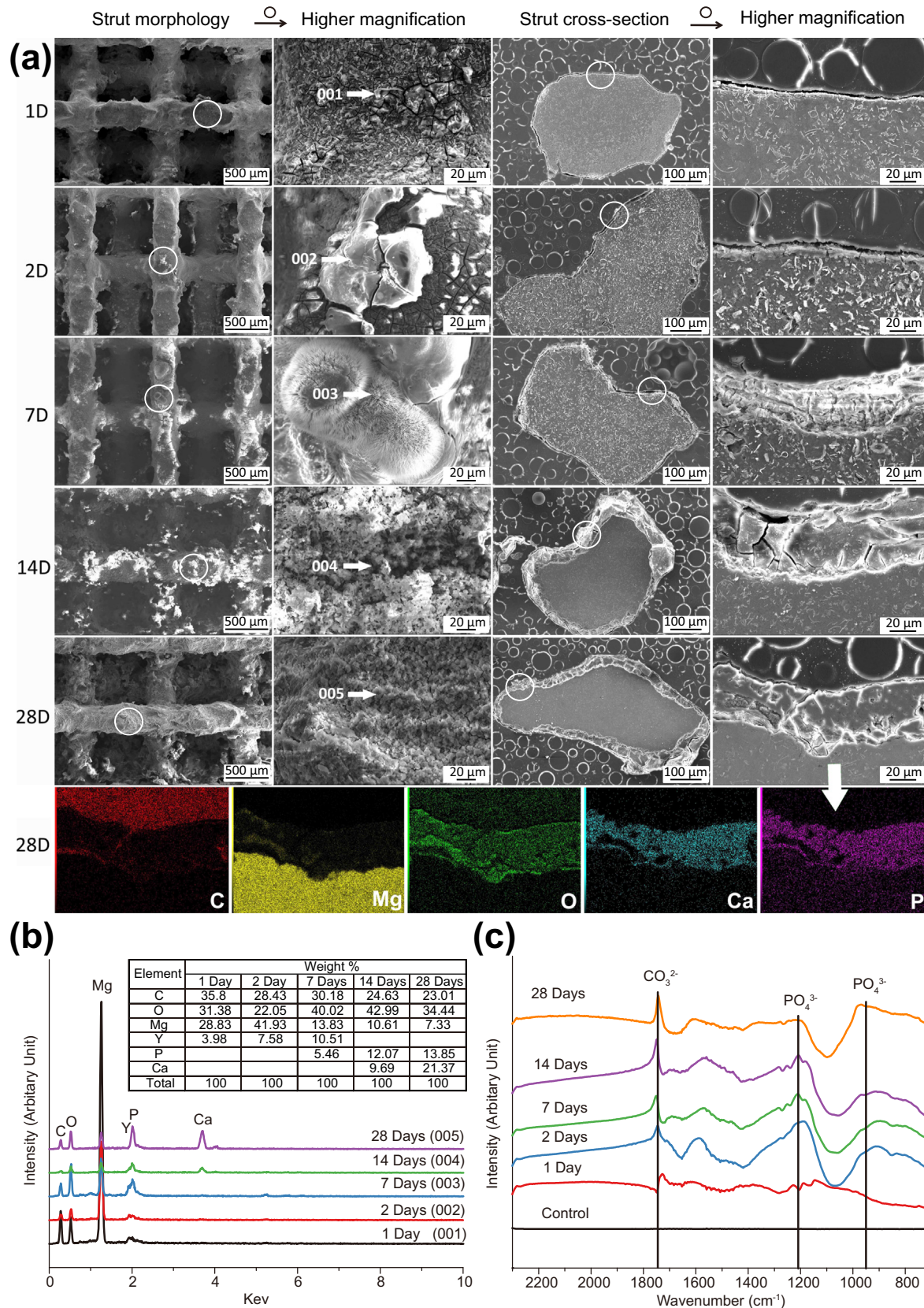
Fig. 4. Characterization of degradation products on the periphery of scaffolds: (a) SEM images and EDS mapping, (b) EDS analysis and (c) FTIR analysis.

(Fig. 8a). The curve started with a linear elastic region, after which its slope rapidly decreased, followed by a plateau stage with fluctuations (Fig. 8a). The final increase in stress corresponded to the densification of the porous structure (Fig. 8a). The differences in Young's modulus and yield strength between the as-built and as-polished samples were insignificant (Fig. 8a). After 1 day and 2
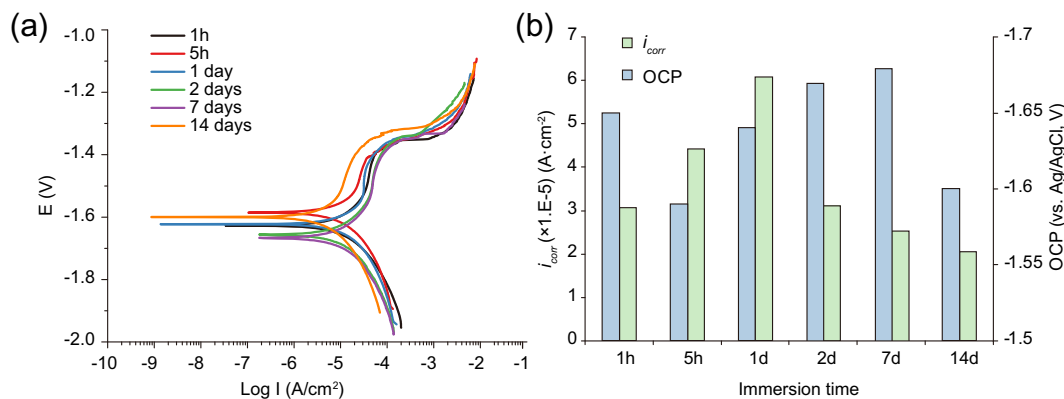
Fig. 5. Electrochemical tests: (a) PDP curves, (b) OCP and corrosion current density change with immersion time.

days, the yield strength decreased and less stress fluctuations were observed after the peak stress as compared to the as-built and as-polished specimens (Fig. 8a). After 7 days, specimens showed almost no plateau stage or densification stage and still less stress fluctuations after the peak stress (Fig. 8a). The Young's modulus increased substantially after 1 day but decreased sharply from day 2 to day 7 (Fig. 8b). The Young's modulus then remained almost unchanged until day 28, while the yield strength showed a moderate decrease from 22 to 20 MPa during the first 14 days (i.e. 9% reduction) and then decreased significantly between day 14 and day 28 from 20 to 13 MPa (i.e. 35% reduction) (Fig. 8c).

3.7. Biocompatibility in vitro

Standardized cell seeding resulted in more (semi-quantitatively) effective cell adherence on Ti-6Al-4V as compared to WE43 (Fig. 9a, d). Live-dead staining with subsequent dual channel fluorescent optical imaging (FOI) showed hardly any cell death on Ti-6Al-4V shortly (i.e., 4 h) after seeding (Fig. 9a), while a significant percentage of MG-63 cells in direct contactwithWE43 appeared to be dying 4 h after immediate seeding (Fig. 9d). The pre-incubation of both scaffolds for 48 h in physiological serum-containing culture medium resulted in a substantial number of cells being viable even after 24 h of direct contact (Fig. 9c, f). Cells in intimate contact with strut surface were detectable by SEM on both materials (Fig. 9c, f). MG-63 cells seemed to adopt different phenotypes on both metal surfaces: on the relatively rough surface of Ti-6Al-4Vspecimens, cells developed a lot of far-stretching filopodia-like protrusions (Fig. 9c, upper arrows). On the eroded WE43 surface (Fig. 9f), cell morphology appeared more condensed, while adherent cells on Ti-6Al-4V appeared larger. After 24 h, few viable (green) cells were detectable on WE43 (Fig. 9f, FOI inlay), while the majority of the cells revealed compromised membrane integrity, being evident from their red fluorescence. The dead-live cell ratio was the opposite on the Ti-6Al-4V scaffolds (Fig. 9c, FOI inlay), showing at least 80% viable cells by semi-quantitative counting (data not shown).

3.8. In vitro cytotoxicity

At the beginning, all treatments revealed close to 100% cellular activity. As expected, for the Sulforaphane group, the cellular activity quickly dropped to about 50% within 24 h and to about 25% after 72 h (Fig. 9g). In contrast, Ti-6Al-4V extracts revealed close to 100% cellular activity at all tested time points, confirming level 0 cytotoxicity (i.e. <25% cytotoxicity, according to ISO) of this material. WE43 extracts revealed similar cytotoxicity, with level 0 cytotoxicity at 75% of the investigated time points (Fig. 9g) with

only the 24 h extracts just reaching level I cytotoxicity (i.e., breaching the >75% viability threshold). At 48 h, however, the cytotoxicity of WE43 extracts was again indistinguishable from that of Ti-6Al-4V extracts (Fig. 9 g).

4. Discussion

The AM porous Mg developed in this work satisfied all the three requirements mentioned in the introduction. First, the mechanical properties of these scaffolds particularly the Young's modulus were high enough to provide mechanical support in a bony environment (E = 700–800 MPa) and were within the range of those reported for trabecular bone (E = 500–20,000 MPa [55]) even after 28 days of biodegradation. Secondly, the actual topology of the porous structures closely matched the designed topology including a fully interconnected porous structure, high porosity, and precisely controlled geometry of the unit cells. Thirdly, AM porous Mg specimens showed a satisfactory biodegradation behavior with ≈20% volume loss after 4 weeks. From a biological viewpoint, they showed only limited cytotoxicity.

4.1. Microstructure

High cooling rates involved in SLM resulted in much smaller grains than those achievable with conventional methods [56]. At the bottom of the struts, the material experienced more cycles of re-melting than that at the top, as a result of the overlapping of the horizontal and vertical scan lines, thereby producing a relatively moderate temperature gradient. The moderate temperature gradient is likely the reason for the development of the rose-like grains, whereas towards the top of struts, rose-like grains became cellular due to a higher temperature gradient [57]. The yttrium-containing second phase particles were uniformly distributed in the microstructure of the α-Mg matrix, probably because laser melting caused temperature gradients in the melt pool that contributed to the formation of strong Marangoni convection and resulted in homogenous dispersion of alloying elements within the melt pool.

4.2. Biodegradation behavior

There are still no standards available concerning the evaluation of the degradation rate of magnesium in vitro. Researchers have developed several methods, such as weight loss measurement, hydrogen evolution measurement, electrochemical methods and μCT. Feyerabend et al. [58] compared these commonly applied methods with their respective advantages and disadvantages. Weight loss measurement is the most widely applied method.
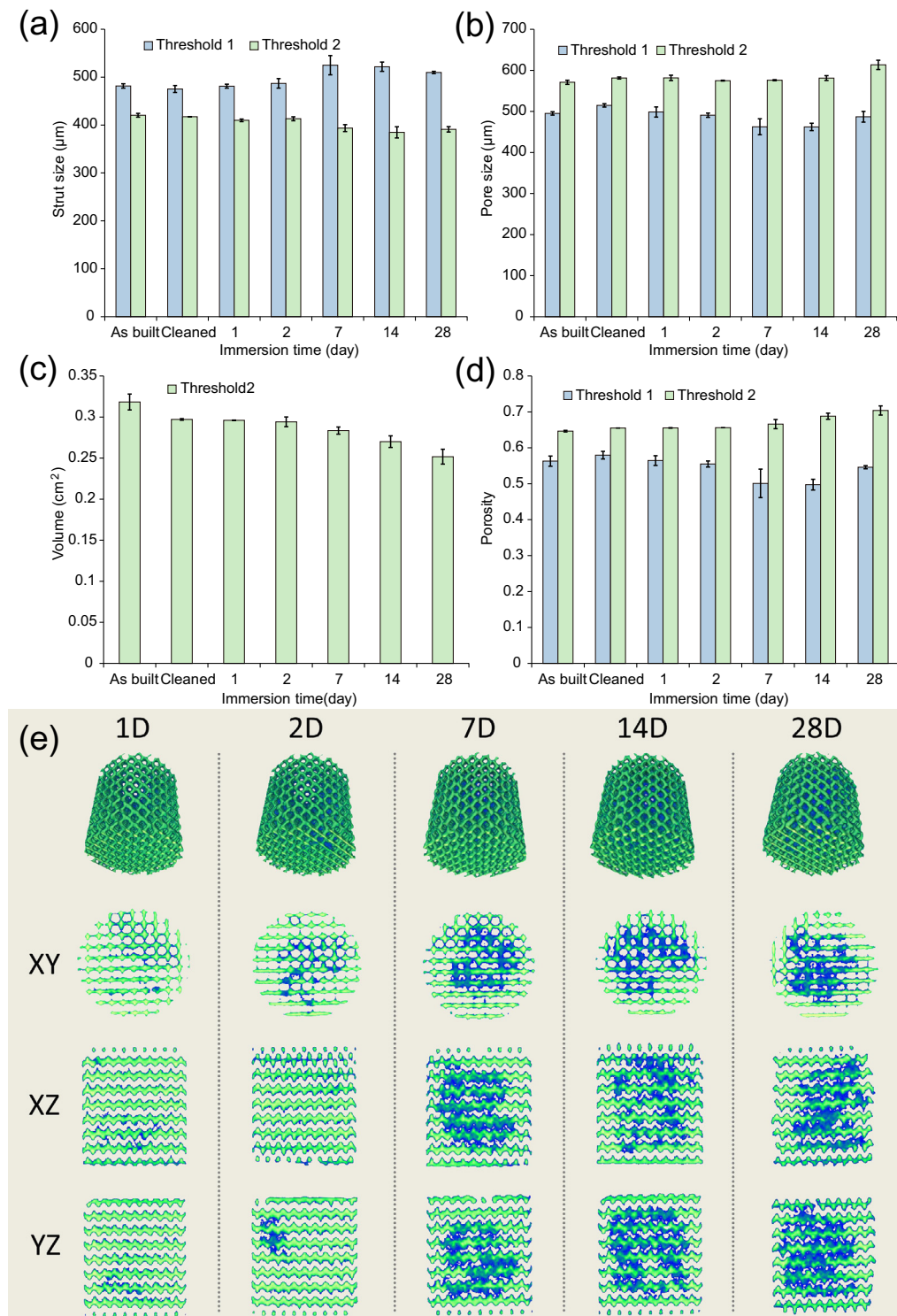
Fig. 6. Micro-CT analysis: (a) strut size, (b) pore size, (c) volume, (d) porosity and (e) 3D reconstruction.

For accurate measurement, the corrosion layers on the magnesium substrate must be carefully and thoroughly removed, usually by using chromic acid, without attacking the magnesium substrate. Our previous controlled experiments to see how much of coatings and surface layers could be removed from AM porous biomaterials have, however, shown that this method is less reliable for volume-porous materials with huge surface areas and relatively small pore sizes. Therefore, in this study, we turned to the other three methods.

In comparison to *in vitro* degradation of conventionally-fabricated counterparts, AM WE43 scaffolds had overall slower hydrogen evolution although temporary increases in corrosion rate occurred a few times over the whole immersion period, which could be attributed to the refined microstructure and complex corrosion mechanisms operating in the scaffolds, in addition to environmental factors. It is therefore clear that the topological design is important when one wishes to adjust the degradation behavior of AM porous Mg.
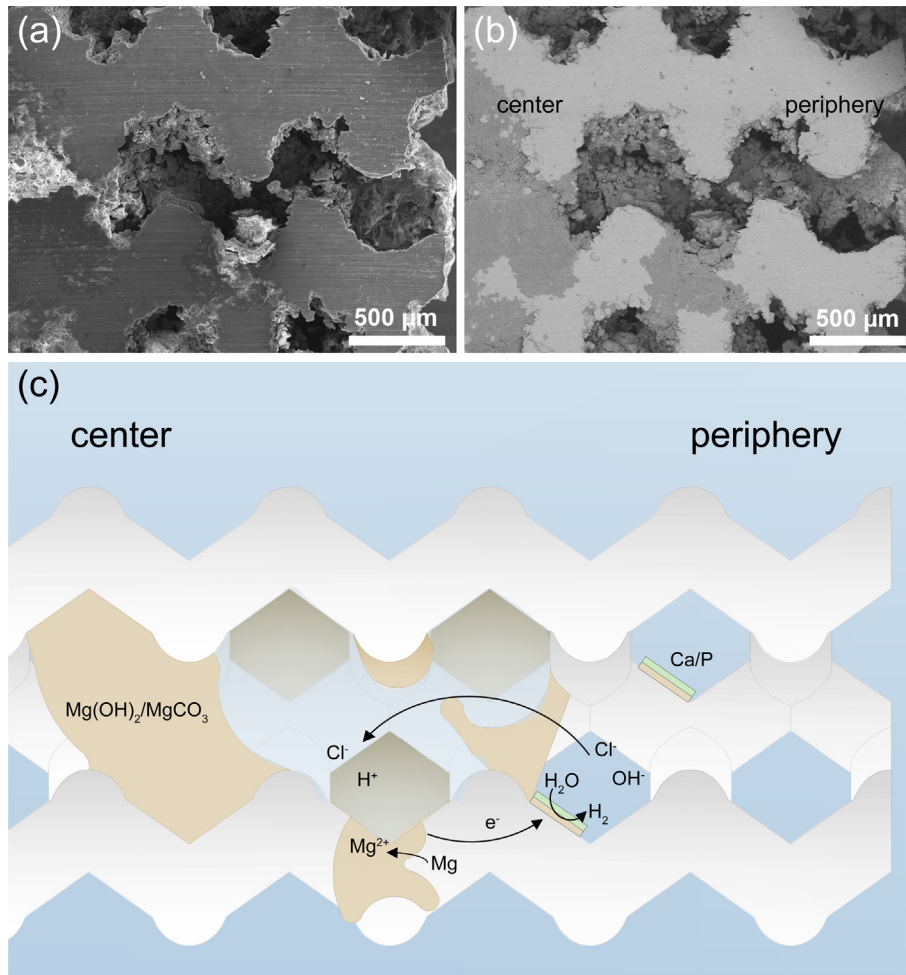
Fig. 7. Macroscopic degradation behavior of scaffolds on the cross-section after 7-day immersion: (a) SEM image, (b) BSE image and (c) schematic illustration of degradation at the center of the WE43 scaffolds.

The biodegradation rate of 0.17 ml/cm^2·day over 4 weeks is lower than the values reported for most cast or extruded WE43 magnesium alloy (i.e., 0.3–2 ml/cm^2·day [25,59–63]). For the interpretation of our *in vitro* degradation results, the immersion test solution matters: r-SBF with 5% FBS. While most researchers used SBF [64] with a high concentration of Cl$^-$ and a low concentration of CO$_3^{2-}$ as compared to r-SBF, the latter has ion concentrations more similar to those in human plasma. Although an addition of 5% FBS to it may have contributed to a decreased corrosion rate *in vitro*, as protein adsorption to the Mg surface may shield it from corrosion [65], this protein concentration is quite subphysiological and supposed to better mimic a vascularized *in vivo* environment. To this end, protein adsorption to implants may be a contributing factor, explaining the overall relatively lower *in vivo* degradation rates of magnesium implants as compared to most *in vitro* results. Furthermore, it is well known that the CO$_2$ content of the immersion medium can influence the outcome of degradation tests [66]. We acknowledge that our experimental set-up is still far away from representing *in vivo* conditions, as we used static conditions in a closed container without CO$_2$ control. Cell metabolism and fluid flow may further influence Mg degradation. These are the limitations of the present study and should be addressed in future projects. Ideally, Mg scaffold degradation should be evaluated in complex *in vitro* environments employing, for example, bioreactors.

In addition to the environmental effects, the fine microstructure of the WE43 alloy resulting from SLM might be a contributor as

well. Although finer grains correspond to a large area of grain boundaries that cause galvanic corrosion, large grain boundaries could act as a more effective physical barrier to corrosion, as compared to coarse grains [67]. In addition, a high fraction of grain boundaries is likely to accelerate passivation kinetics and reduce the intensity of micro galvanic coupling between grains and grain boundaries [68,69]. Furthermore, the homogeneously distributed second phase in the grain interior also favors the uniform corrosion of grains [70,71] and the galvanic corrosion triggered by these second phase particles may be compromised by later-on formed corrosion layers.

To reveal the corrosion mechanisms of the WE43 scaffolds, we further investigated the corrosion behavior from micro to macro scales. At the micro level, the presented results (SEM, FTIR, OCP and PDP) suggested the gradual formation of corrosion layer with time. At the beginning of *in vitro* immersion, the magnesium matrix dissolved as the anode, making the flake-shaped second phase embossed, because the second phase is nobler and less reactive than the magnesium matrix. Simultaneously, hydrogen was produced through a cathodic reaction, which resulted in a local alkaline environment. The formation of a magnesium hydroxide Mg(OH)$_2$ layer on the magnesium surface acted as a protective barrier to further corrosion. This corresponds to the OCP value shifting to more positive potential after 5-h immersion. However, Mg(OH)$_2$ is not stable and could be transformed into soluble MgCl$_2$ in the solution containing chloride ions [72]. That is why the OCP value of the 1-day immersion specimen was even more negative than
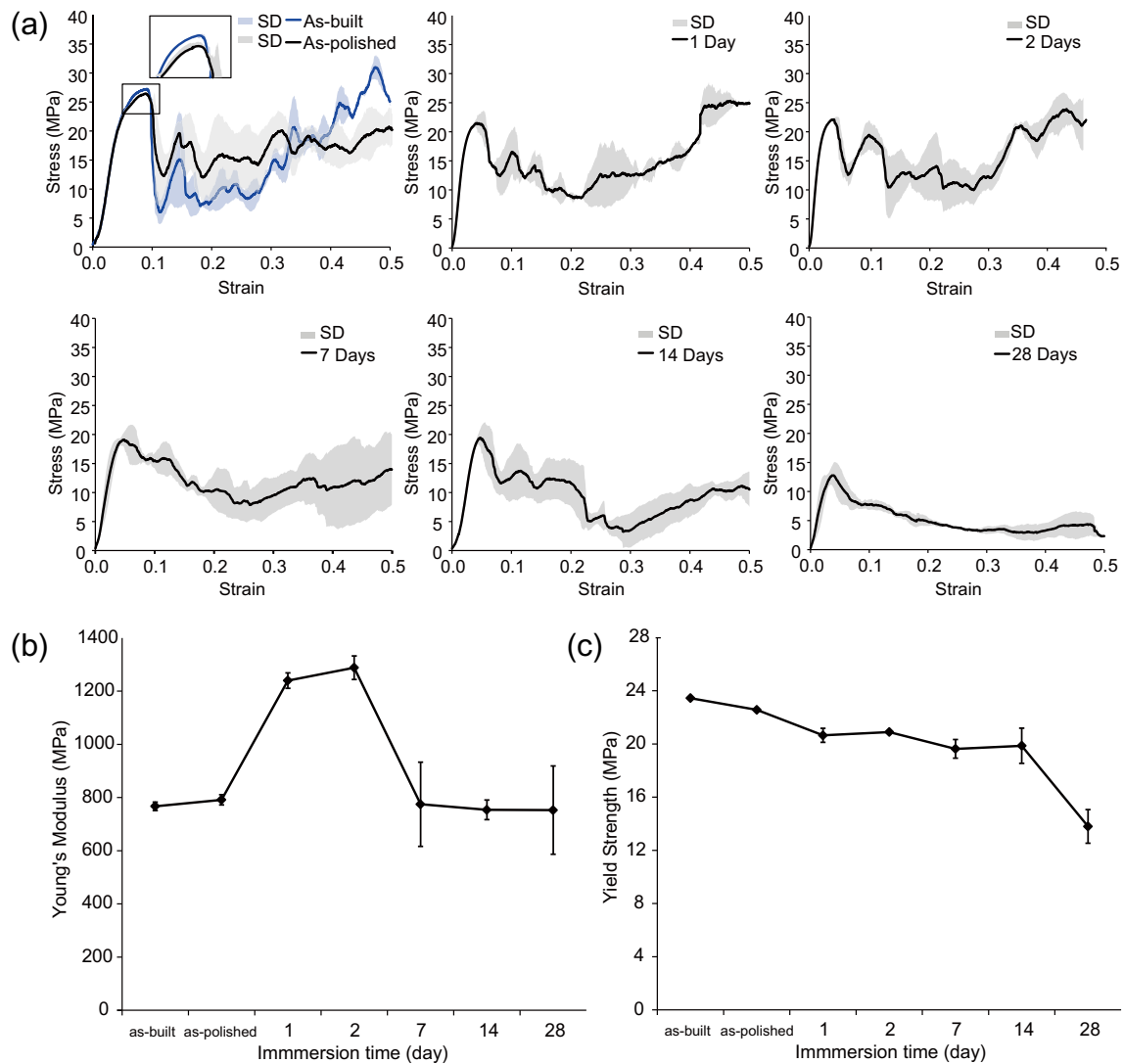
Fig. 8. Mechanical behavior: (a) compressive stress-strain curves, (b) stiffness change with immersion time and (c) yield strength change with immersion time.

the 5-h immersion. After 1 day, the rupture and formation of this layer competed with each other. At the same time, carbonates and phosphates started to form on the surface around the second-phase particles. Thereafter, an apatite-like material formed because the previously formed passive layer provided favorable sites for apatite nucleation and its continuous growth was maintained by consuming Ca and P species in the surrounding solution [73]. The formation of less soluble precipitates explains the potential increase and i_{corr} values decrease from day 2 onwards. After a longer immersion time, an equilibrium between the formation and dissolution of degradation products was established.

At the macro level, μCT and BSE analyses suggest that the scaffolds experienced uniform corrosion at the periphery and a localized corrosion in the center. Hydrogen released very fast at the beginning and then slowed down due to the formation of a passive corrosion layer. As corrosion proceeded, localized corrosion contributed more than uniform corrosion to overall corrosion and hydrogen release rate increased several times after day 3. Besides, hydrogen bubbles entrapped inside the scaffolds might have influenced the measurable hydrogen release rate. Logically, the pH value of the solution increased more in the center of the scaffolds as compared to the periphery, which made the degradation layer more stable in the center. The accumulation of degradation products between the struts created relatively narrow spaces that could

lead to limited diffusion of Mg ions in the center where crevice-like corrosion might occur (Fig. 7c), which resulted in the build-up of Mg ions with a concentration gradient set up between the entrance and the end of the space. Then, the negatively charged Cl ions migrated into the narrow space under the attraction of the positively charge Mg ions. Hydrolysis of chloride lowered pH and breached the passive layer locally inside the narrow space. At the same time, the periphery of the specimens with a passive layer might act as a cathode, building a corrosion cell with the magnesium alloy inside the scaffolds, which further accelerated the corrosion in the center (Fig. 7c). In addition to the crevice-like corrosion mechanism, the difference in surface roughness of struts between the periphery and center of the scaffolds could lead to different corrosion behaviors, although the exact effect is still debatable, as opposite results have been obtained [74]. The differentiated corrosion rates and corrosion mechanisms between the scaffold center and periphery indicate that in addition to the choice of material, the design of open porous structures is of great importance and an optimum scaffold design should take these factors into account.

4.3. Mechanical behavior

During degradation, the specimens may be considered as a composite material composed of metal (magnesium) and ceramics
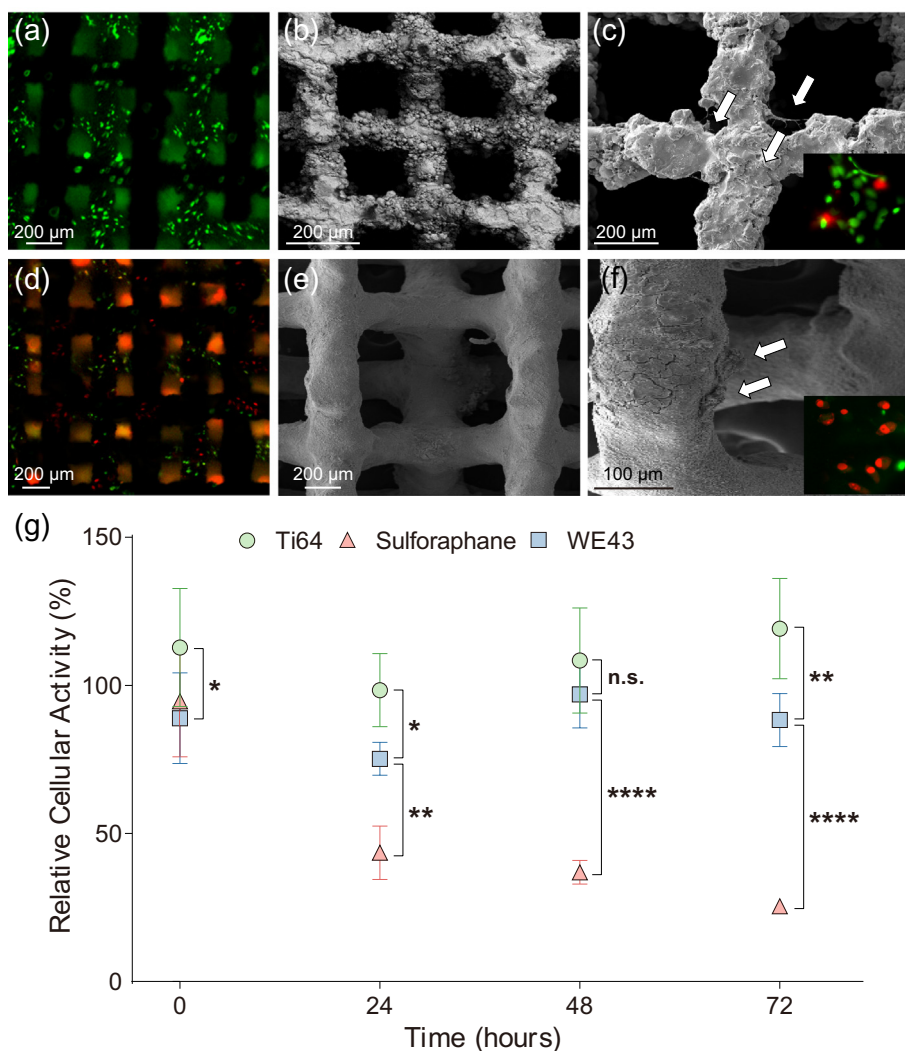
Fig. 9. Biocompatibility and cytotoxicity of AM scaffolds *in vitro*: (a), (d) low magnification fluorescent optical images (FOI) of MG-63cells on Ti-6Al-4V (a) and WE43 (d) scaffolds 4 h after seeding, (b), (e) higher magnification SEM of Ti-6Al-4V (b) and WE43 (e) scaffolds before seeding, (c), (f) SEM and FOI of Ti-6Al-4V (c) and WE43 (f) scaffolds 24 h after seeding (arrows indicate individual cells: live cells, green; dead cells, red), (g) cytotoxicity screening of scaffolds *in vitro*, experiments were performed with extracts of randomly chosen replicate scaffolds ($n = 5$) and analyzed in at least technical triplicates (WE43, $n = 5$; Ti-6Al-4V, $n = 3$). (For interpretation of the references to colour in this figure legend, the reader is referred to the web version of this article.)

(degradation products). The corrosion appeared to influence the stiffness differently from the yield strength. That is perhaps related to the different influence of interfacial bonding, which is between the degradation products and magnesium alloy in our case, on the Young's modulus and yield strength of a composite material [75]. Since the Young's modulus was measured at relatively low deformation, there was insufficient dilation to cause interface separation and the load could still be carried by these two phases. As a result, the Young's modulus of the WE43 scaffolds increased with increasing amount of degradation products. After localized corrosion occurred around day 7, the Young's modulus of the scaffolds was not only affected by the amount of degradation products but also by the structural changes within the scaffolds. The Young's modulus of 7-day specimen decreased to a value similar to that measured before immersion, because localized corrosion could lead to stress concentrations in some severely degraded struts. For the yield strength of a composite structure, interfacial bonding is of particular importance, especially at strains close to the yield point. For poorly bonded degradation products, stress transfer at the degradation product/magnesium interface may be inefficient, the degradation products cannot carry much of the load and thus

the yield strength is primarily dependent on the strength of the remaining magnesium. As a result, the strength of the degraded scaffolds decreased with increasing amounts of degradation products and the decreasing amount of magnesium alloy along with biodegradation.

4.4. Biological evaluation

Only 24 h WE43 extracts revealed cytotoxicity level I by MTS analysis, while all other extracts fulfilled cytotoxicity level 0 requirements. The longest recommended 72 h extraction period [76] showed less than 25% cytotoxicity, similar to our positive control, i.e., Ti-6Al-4V extracts. To avoid any interference of corroded magnesium with tetrazolium salt by converting it into formazan [76,77],we followed established procedures and replaced culture media [76] prior to adding the MTS reagent. We further used Sulforaphane (10 µM) as an established cytotoxic (i.e., negative) control in the MTS assay, confirming earlier data [50].

We noticed morphological changes in MG-63 cells after 24 h of contact to both WE43 and Ti-6Al-4V. Similar observations have been reported by Li et al. [78] who compared the biocompatibility

of titanium rods with that of pure and oxidized magnesium rods (solid). The authors did hardly find live MG-63 cells on pure Mg after 24 h of incubation, while micro-arc oxidized Mg had a much weaker cytotoxic effect, but slightly stronger than that of titanium. This is in good agreement with our data as the 48 h *in vitro* pre-incubation of our WE43 scaffolds prior to cell seeding may have resulted in a protective surface coating of immature 'hydroxyapatite' and serum proteins. Many systematic corrosion studies on magnesium alloys with different corrosion media are reported, with the composition of the corrosion media always influencing the Mg corrosion behavior. Proteins such as albumin, are known to form a corrosion-blocking layer on Mg alloys *in vitro* [79,80], which usually is enriched in calcium and phosphates from the culture medium [79,80]. While real hydroxyapatite would unlikely form under these conditions, even immature apatite-like layers concomitantly would participate in corrosion protection [81], which was also evident from our own corrosion data in the present study.

Direct contact evaluation *in vitro* suggests that WE43 may not *per se* be an ideal substrate to grow MG-63 cells on. However, cytotoxicity testing based on ISO 10993-5 and -12 standards was initially intended for non-degradable metals and (degradable) polymers [82]. An increasing body of evidence now suggests that these standards may be inappropriate for evaluating biodegradable less than 75% cell viability *in vitro* is reported [82]. Importantly, this is in sharp contrast to very promising *in vivo* findings [83,84]. It is important to realize that, in contrast to the *in vitro* environment, the released magnesium and hydroxyl ions are promptly diluted *in vivo* by the surrounding body fluid and diffuse into circulation to be rapidly excreted from the body. To better mimic the *in vivo* situation, the latest recommendation is to use a 10-times higher extraction ratio [48,51] as the 0.2 g/mL specimen-to-weight extraction ratio suggested by EN ISO 10993-5 and 10993-12. The latter extracts appeared reasonably safe based on our cell activity data (Fig. 9 g) and are in good agreement with our pH measurements, revealing sharp differences between the pH values at the scaffold surface as compared to those in the bulk medium. Undiluted extracts from WE43also have high osmolality, while 400 mOsm/kgor less is well tolerated by primary osteoblasts and MG-63 cells alike [51]. Of note, our highly porous WE43 scaffolds further have a very large surface area (25.4 cm^2) as compared to earlier tested solid materials, but still never revealed more than 25% of viability loss. *In vivo*, the human body actively regulates local changes in the pH, osmolality, and hydrogen levels by interstitial transport. Comprehensive *in vitro* and *in vivo* studies are therefore needed to better understand the biological performance of AM WE43. In addition, according to data given by Zheng et al. [20], the daily allowance of Mg in the human body is 700 mg while the highest daily Mg ion release in our immersion tests was only 13 mg at day 1, which means, theoretically, 50 times larger scaffolds (in volume) than the current one (10 * 11.2 mm) could still be safely implanted.

5. Conclusions

We used AM to fabricate biodegradable porous Mg that has the potential to satisfy all the functional requirements regarding an ideal bone substituting material. First, its mechanical properties are high enough for proper mechanical support and within those reported for trabecular bone even after 4 weeks of biodegradation. Secondly, they present a fully interconnected porous structure with precise control over topology. Thirdly, the biodegradation rate of the biomaterials is satisfactory with ≈20% volume loss after 4 weeks. Moreover, WE43 scaffolds revealed less than 25% cytotoxicity *in vitro*. Although pure WE43 itself may not be an ideal surface

for cell adhesion, with the right design and coating, Mg-based biomaterials could be part of a new generation of functional degradable biomaterials, particularly in orthopedic applications.

References

[1] S. Van Bael, Y.C. Chai, S. Truscello, M. Moesen, G. Kerckhofs, H. Van Oosterwyck, J.P. Kruth, J. Schrooten, The effect of pore geometry on the in vitro biological behavior of human periosteum-derived cells seeded on selective laser-melted Ti6Al4V bone scaffolds, Acta Biomater. 8 (2012) 2824–2834.

[2] A. Oryan, S. Alidadi, A. Moshiri, N. Maffulli, Bone regenerative medicine: classic options, novel strategies, and future directions, J. Orthopaed. Surg. Res. 9 (2014) 18.

[3] I.-H. Oh, N. Nomura, N. Masahashi, S. Hanada, Mechanical properties of porous titanium compacts prepared by powder sintering, Scr. Mater. 49 (2003) 1197–1202.

[4] C.E. Wen, M. Mabuchi, Y. Yamada, K. Shimojima, Y. Chino, T. Asahina, Processing of biocompatible porous Ti and Mg, Scr. Mater. 45 (2001) 1147–1153.

[5] A.A. Zadpoor, Bone tissue regeneration: the role of scaffold geometry, Biomater. Sci. 3 (2015) 231–245.

[6] Y. Chen, Z. Xu, C. Smith, J. Sankar, Recent advances on the development of magnesium alloys for biodegradable implants, Acta Biomater. 10 (2014) 4561–4573.

[7] A.A. Zadpoor, Mechanics of additively manufactured biomaterials, J. Mech. Behav. Biomed. Mater. 70 (2017) 1–6.

[8] X. Wang, S. Xu, S. Zhou, W. Xu, M. Leary, P. Choong, M. Qian, M. Brandt, Y.M. Xie, Topological design and additive manufacturing of porous metals for bone scaffolds and orthopaedic implants: a review, Biomaterials 83 (2016) 127–141.

[9] F.S.L. Bobbert, K. Lietaert, A.A. Eftekhari, B. Pouran, S.M. Ahmadi, H. Weinans, A. Zadpoor, Additively manufactured metallic porous biomaterials based on minimal surfaces: a unique combination of topological, mechanical, and mass transport properties, Acta Biomater. 53 (2017) 572–584.

[10] J. Van der Stok, O.P. Van der Jagt, S. Amin Yavari, M.F.P. De Haas, J.H. Waarsing, H. Jahr, E.M.M. Van Lieshout, P. Patka, J.A.N. Verhaar, A.A. Zadpoor, H. Weinans, Selective laser melting-produced porous titanium scaffolds regenerate bone in critical size cortical bone defects, J. Orthop. Res. 31 (2013) 792–799.

[11] S. Ahmadi, S. Yavari, R. Wauthle, B. Pouran, J. Schrooten, H. Weinans, A. Zadpoor, Additively manufactured open-cell porous biomaterials made from six different space-filling unit cells: the mechanical and morphological properties, Materials 8 (2015) 1871.

[12] C. Yan, L. Hao, A. Hussein, P. Young, D. Raymont, Advanced lightweight 316L stainless steel cellular lattice structures fabricated via selective laser melting, Mater. Des. 55 (2014) 533–541.

[13] R. Wauthle, J. van der Stok, S. Amin Yavari, J. Van Humbeeck, J.-P. Kruth, A.A. Zadpoor, H. Weinans, M. Mulier, J. Schrooten, Additively manufactured porous tantalum implants, Acta Biomater. 14 (2015) 217–225.

[14] S. Limmahakhun, A. Oloyede, K. Sitthiseripratip, Y. Xiao, C. Yan, Stiffness and strength tailoring of cobalt chromium graded cellular structures for stress-shielding reduction, Mater. Des. 114 (2017) 633–641.

[15] I.A. van Hengel, M. Riool, L.E. Fratila-Apachitei, J. Witte-Bouma, E. Farrell, A.A. Zadpoor, S.A. Zaat, I. Apachitei, Selective laser melting porous metallic implants with immobilized silver nanoparticles kill and prevent biofilm formation by methicillin-resistant Staphylococcus aureus, Biomaterials (2017).

[16] M. Moravej, D. Mantovani, Biodegradable metals for cardiovascular stent application: interests and new opportunities, Int. J. Mol. Sci. 12 (2011) 4250.

[17] F. Witte, The history of biodegradable magnesium implants: a review, Acta Biomater. 6 (2010) 1680–1692.

[18] C. Palacios, The role of nutrients in bone health, from A to Z, Crit. Rev. Food Sci. Nutr. 46 (2006) 621–628.

[19] M.P. Staiger, A.M. Pietak, J. Huadmai, G. Dias, Magnesium and its alloys as orthopedic biomaterials: a review, Biomaterials 27 (2006) 1728–1734.

[20] Y.F. Zheng, X.N. Gu, F. Witte, Biodegradable metals, Mater. Sci. Eng.: R: Rep. 77 (2014) 1–34.

[21] B. Zberg, P.J. Uggowitzer, J.F. Loffler, MgZnCa glasses without clinically observable hydrogen evolution for biodegradable implants, Nat. Mater. 8 (2009) 887–891.

[22] Q. Peng, Y. Huang, L. Zhou, N. Hort, K.U. Kainer, Preparation and properties of high purity Mg–Y biomaterials, Biomaterials 31 (2010) 398–403.

[23] N. Hort, Y. Huang, D. Fechner, M. Störmer, C. Blawert, F. Witte, C. Vogt, H. Drücker, R. Willumeit, K.U. Kainer, F. Feyerabend, Magnesium alloys as implant materials – principles of property design for Mg–RE alloys, Acta Biomater. 6 (2010) 1714–1725.

[24] D.-T. Chou, D. Hong, P. Saha, J. Ferrero, B. Lee, Z. Tan, Z. Dong, P.N. Kumta, In vitro and in vivo corrosion, cytocompatibility and mechanical properties of biodegradable Mg–Y–Ca–Zr alloys as implant materials, Acta Biomater. 9 (2013) 8518–8533.

[25] A.C. Hänzi, P. Gunde, M. Schinhammer, P.J. Uggowitzer, On the biodegradation performance of an Mg–Y–RE alloy with various surface conditions in simulated body fluid, Acta Biomater. 5 (2009) 162–171.

[26] C. Di Mario, H.U.W. Griffiths, O. Goktekin, N. Peeters, J.A.N. Verbist, M. Bosiers, K. Deloose, B. Heublein, R. Rohde, V. Kasese, C. Ilsley, R. Erbel, Drug-eluting bioabsorbable magnesium stent, J. Interventional Cardiol. 17 (2004) 391–395.

[27] R. Erbel, C. Di Mario, J. Bartunek, J. Bonnier, B. de Bruyne, F.R. Eberli, P. Erne, M. Haude, B. Heublein, M. Horrigan, C. Ilsley, D. Böse, J. Koolen, T.F. Lüscher, N. Weissman, R. Waksman, Temporary scaffolding of coronary arteries with bioabsorbable magnesium stents: a prospective, non-randomised multicentre trial, Lancet 369 (2007) 1869–1875.

[28] M. Haude, R. Erbel, P. Erne, S. Verheye, H. Degen, D. Böse, P. Vermeersch, I. Wijnbergen, N. Weissman, F. Prati, R. Waksman, J. Koolen, Safety and performance of the drug-eluting absorbable metal scaffold (DREAMS) in patients with de-novo coronary lesions: 12 month results of the prospective, multicentre, first-in-man BIOSOLVE-I trial, Lancet 381 (2013) 836–844.

[29] K. Bobe, E. Willbold, I. Morgenthal, O. Andersen, T. Studnitzky, J. Nellesen, W. Tillmann, C. Vogt, K. Vano, F. Witte, In vitro and in vivo evaluation of biodegradable, open-porous scaffolds made of sintered magnesium W4 short fibres, Acta Biomater. 9 (2013) 8611–8623.

[30] Z. Chen, X. Mao, L. Tan, T. Friis, C. Wu, R. Crawford, Y. Xiao, Osteoimmunomodulatory properties of magnesium scaffolds coated with β-tricalcium phosphate, Biomaterials 35 (2014) 8553–8565.

[31] M.-Q. Cheng, T. Wahafu, G.-F. Jiang, W. Liu, Y.-Q. Qiao, X.-C. Peng, T. Cheng, X.-L. Zhang, G. He, X.-Y. Liu, A novel open-porous magnesium scaffold with controllable microstructures and properties for bone regeneration, Sci. Rep. 6 (2016) 24134.

[32] G. Jiang, G. He, A new approach to the fabrication of porous magnesium with well-controlled 3D pore structure for orthopedic applications, Mater. Sci. Eng. C 43 (2014) 317–320.

[33] A.P. Md Saad, R.A. Abdul Rahim, M.N. Harun, H. Basri, J. Abdullah, M.R. Abdul Kadir, A. Syahrom, The influence of flow rates on the dynamic degradation behaviour of porous magnesium under a simulated environment of human cancellous bone, Mater. Des. 122 (2017) 268–279.

[34] A.P.Md. Saad, N. Jasmawati, M.N. Harun, M.R. Abdul Kadir, H. Nur, H. Hermawan, A. Syahrom, Dynamic degradation of porous magnesium under a simulated environment of human cancellous bone, Corros. Sci. 112 (2016) 495–506.

[35] I. Morgenthal, O. Andersen, C. Kostmann, G. Stephani, T. Studnitzky, F. Witte, B. Kieback, Highly porous magnesium alloy structures and their properties regarding degradable implant application, Adv. Eng. Mater. 16 (2014) 309–318.

[36] F. Witte, H. Ulrich, C. Palm, E. Willbold, Biodegradable magnesium scaffolds: Part II: peri-implant bone remodeling, J. Biomed. Mater. Res. Part A 81 (2007) 757–765.

[37] F. Witte, H. Ulrich, M. Rudert, E. Willbold, Biodegradable magnesium scaffolds: Part 1: appropriate inflammatory response, J. Biomed. Mater. Res. Part A 81 (2007) 748–756.

[38] X. Zhang, X.-W. Li, J.-G. Li, X.-D. Sun, Preparation and mechanical property of a novel 3D porous magnesium scaffold for bone tissue engineering, Mater. Sci. Eng., C 42 (2014) 362–367.

[39] H. Zhuang, Y. Han, A. Feng, Preparation, mechanical properties and in vitro biodegradation of porous magnesium scaffolds, Mater. Sci. Eng., C 28 (2008) 1462–1466.

[40] T.L. Nguyen, M.P. Staiger, G.J. Dias, T.B.F. Woodfield, A novel manufacturing route for fabrication of topologically-ordered porous magnesium scaffolds, Adv. Eng. Mater. 13 (2011) 872–881.

[41] A.A. Zadpoor, J. Malda, Additive Manufacturing of Biomaterials, Tissues, and Organs, Springer, 2017.

[42] D. Hu, Y. Wang, D. Zhang, L. Hao, J. Jiang, Z. Li, Y. Chen, Experimental investigation on selective laser melting of bulk net-shape pure magnesium, Mater. Manuf. Processes 30 (2015) 1298–1304.

[43] C.C. Ng, M. Savalani, H.C. Man, Fabrication of magnesium using selective laser melting technique, Rapid Prototyp. J. 17 (2011) 479–490.

[44] Y. Yang, P. Wu, X. Lin, Y. Liu, H. Bian, Y. Zhou, C. Gao, C. Shuai, System development, formability quality and microstructure evolution of selective laser-melted magnesium, Virtual Phys. Prototyp. 11 (2016) 173–181.

[45] L. Jauer, B. Jülich, M. Voshage, W. Meiners, Selective laser melting of magnesium alloys, Eur. Cells Mater. 30 (2015).

[46] F. Witte, L. Jauer, W. Meiners, Z. Kronbach, K. Strohschein, T. Schmidt, Open-porous biodegradable magnesium scaffolds produced by selective laser melting for individualized bone replacement, Front. Bioeng. Biotechnol. 4 (2016).

[47] A. Oyane, H.-M. Kim, T. Furuya, T. Kokubo, T. Miyazaki, T. Nakamura, Preparation and assessment of revised simulated body fluids, J. Biomed. Mater. Res. Part A 65A (2003) 188–195.

[48] J. Wang, F. Witte, T. Xi, Y. Zheng, K. Yang, Y. Yang, D. Zhao, J. Meng, Y. Li, W. Li, K. Chan, L. Qin, Recommendation for modifying current cytotoxicity testing standards for biodegradable magnesium-based materials, Acta Biomater. 21 (2015) 237–249.

[49] J. van der Stok, M. Koolen, M. de Maat, S.A. Yavari, J. Alblas, P. Patka, J. Verhaar, E. van Lieshout, A.A. Zadpoor, H. Weinans, Full regeneration of segmental bone defects using porous titanium implants loaded with BMP-2 containing fibrin gels, Eur. Cells Mater. 2015 (2015) 141–154.

[50] J.M.P. Ferreira de Oliveira, C. Remédios, H. Oliveira, P. Pinto, F. Pinho, S. Pinho, M. Costa, C. Santos, Sulforaphane induces DNA damage and mitotic abnormalities in human osteosarcoma MG-63 cells: correlation with cell cycle arrest and apoptosis, Nutr. Cancer 66 (2014) 325–334.

[51] J. Fischer, D. Pröfrock, N. Hort, R. Willumeit, F. Feyerabend, Reprint of: Improved cytotoxicity testing of magnesium materials, Mater. Sci. Eng., B 176 (2011) 1773–1777.

[52] R. Beckmann, A. Houben, M. Tohidnezhad, A. Kweider, C. Fragoulis, C. Wruck, L. Brandenburg, B. Hermanns-Sachweh, M. Goldring, T. Pufe, H. Jahr, Mechanical forces induce changes in VEGF and VEGFR-1/sFlt-1 expression in human chondrocytes, Int. J. Mol. Sci. 15 (2014) 15456.

[53] I. Rehman, W. Bonfield, Characterization of hydroxyapatite and carbonated apatite by photo acoustic FTIR spectroscopy, J. Mater. Sci. Mater. Med. 8 (1997) 1–4.

[54] A.C. Taş, P.J. Majewski, F. Aldinger, Chemical preparation of pure and strontium-and/or magnesium-doped lanthanum gallate powders, J. Am. Ceram. Soc. 83 (2000) 2954–2960.

[55] J. Parthasarathy, B. Starly, S. Raman, A. Christensen, Mechanical evaluation of porous titanium (Ti6Al4V) structures with electron beam melting (EBM), J. Mech. Behav. Biomed. Mater. 3 (2010) 249–259.

[56] C.C. Ng, M.M. Savalani, M.L. Lau, H.C. Man, Microstructure and mechanical properties of selective laser melted magnesium, Appl. Surf. Sci. 257 (2011) 7447–7454.

[57] V. Manakari, G. Parande, M. Gupta, Selective laser melting of magnesium and magnesium alloy powders: a review, Metals 7 (2016) 2.

[58] F. Feyerabend, In vitro analysis of magnesium corrosion in orthopaedic biomaterials, in: P. Dubruel, S. van Vlierberghe (Eds.), Biomaterials for Bone Regeneration, Woodhead Publishing, Cambridge UK, 2014, pp. 225–269.

[59] F. Witte, J. Fischer, J. Nellesen, H.-A. Crostack, V. Kaese, A. Pisch, F. Beckmann, H. Windhagen, In vitro and in vivo corrosion measurements of magnesium alloys, Biomaterials 27 (2006) 1013–1018.

[60] X.N. Gu, W.R. Zhou, Y.F. Zheng, Y. Cheng, S.C. Wei, S.P. Zhong, T.F. Xi, L.J. Chen, Corrosion fatigue behaviors of two biomedical Mg alloys – AZ91D and WE43 – in simulated body fluid, Acta Biomater. 6 (2010) 4605–4613.

[61] A.C. Hänzi, I. Gerber, M. Schinhammer, J.F. Löffler, P.J. Uggowitzer, On the in vitro and in vivo degradation performance and biological response of new biodegradable Mg–Y–Zn alloys, Acta Biomater. 6 (2010) 1824–1833.

[62] W. Jin, G. Wu, H. Feng, W. Wang, X. Zhang, P.K. Chu, Improvement of corrosion resistance and biocompatibility of rare-earth WE43 magnesium alloy by neodymium self-ion implantation, Corros. Sci. 94 (2015) 142–155.

[63] M.A. Leeflang, J.S. Dzwonczyk, J. Zhou, J. Duszczyk, Long-term biodegradation and associated hydrogen evolution of duplex-structured Mg–Li–Al–(RE) alloys and their mechanical properties, Mater. Sci. Eng., B 176 (2011) 1741–1745.

[64] T. Kokubo, H. Takadama, How useful is SBF in predicting in vivo bone bioactivity?, Biomaterials 27 (2006) 2907–2915

[65] C. Liu, Y. Xin, X. Tian, P.K. Chu, Degradation susceptibility of surgical magnesium alloy in artificial biological fluid containing albumin, J. Mater. Res. 22 (2011) 1806–1814.

[66] R. Willumeit, J. Fischer, F. Feyerabend, N. Hort, U. Bismayer, S. Heidrich, B. Mihailova, Chemical surface alteration of biodegradable magnesium exposed to corrosion media, Acta Biomater. 7 (2011) 2704–2715.

[67] N.N. Aung, W. Zhou, Effect of grain size and twins on corrosion behaviour of AZ31B magnesium alloy, Corros. Sci. 52 (2010) 589–594.

[68] G.R. Argade, S.K. Panigrahi, R.S. Mishra, Effects of grain size on the corrosion resistance of wrought magnesium alloys containing neodymium, Corros. Sci. 58 (2012) 145–151.

[69] M. Alvarez-Lopez, M.D. Pereda, J.A. del Valle, M. Fernandez-Lorenzo, M.C. Garcia-Alonso, O.A. Ruano, M.L. Escudero, Corrosion behaviour of AZ31 magnesium alloy with different grain sizes in simulated biological fluids, Acta Biomater. 6 (2010) 1763–1771.

[70] A. Atrens, G.-L. Song, M. Liu, Z. Shi, F. Cao, M.S. Dargusch, Review of recent developments in the field of magnesium corrosion, Adv. Eng. Mater. 17 (2015) 400–453.

[71] G.v. Baril, C. Blanc, N. Pébère, AC impedance spectroscopy in characterizing time-dependent corrosion of AZ91 and AM50 magnesium alloys characterization with respect to their microstructures, J. Electrochem. Soc. 148 (2001) B489.

[72] M. Esmaily, J.E. Svensson, S. Fajardo, N. Birbilis, G.S. Frankel, S. Virtanen, R. Arrabal, S. Thomas, L.G. Johansson, Fundamentals and advances in magnesium alloy corrosion, Prog. Mater Sci. 89 (2017) 92–193.

[73] Y. Xin, T. Hu, P.K. Chu, Degradation behaviour of pure magnesium in simulated body fluids with different concentrations of HCO3, Corros. Sci. 53 (2011) 1522–1528.

[74] X. Li, X. Liu, S. Wu, K.W.K. Yeung, Y. Zheng, P.K. Chu, Design of magnesium alloys with controllable degradation for biomedical implants: from bulk to surface, Acta Biomater. 45 (2016) 2–30.

[75] S.-Y. Fu, X.-Q. Feng, B. Lauke, Y.-W. Mai, Effects of particle size, particle/matrix interface adhesion and particle loading on mechanical properties of particulate–polymer composites, Compos. B Eng. 39 (2008) 933–961.

[76] J. Fischer, M.H. Prosenc, M. Wolff, N. Hort, R. Willumeit, F. Feyerabend, Interference of magnesium corrosion with tetrazolium-based cytotoxicity assays, Acta Biomater. 6 (2010) 1813–1823.

[77] M. Yazdimamaghani, M. Razavi, D. Vashaee, K. Moharamzadeh, A.R. Boccaccini, L. Tayebi, Porous magnesium-based scaffolds for tissue engineering, Mater. Sci. Eng., C 71 (2017) 1253–1266.

[78] M. Li, L. Ren, L. Li, P. He, G. Lan, Y. Zhang, K. Yang, Cytotoxic effect on osteosarcoma MG-63 cells by degradation of magnesium, J. Mater. Sci. Technol. 30 (2014) 888–893.

[79] R. Rettig, S. Virtanen, Time-dependent electrochemical characterization of the corrosion of a magnesium rare-earth alloy in simulated body fluids, J. Biomed. Mater. Res. Part A 85A (2008) 167–175.

[80] C. Liu, Y. Xin, X. Tian, P.K. Chu, Degradation susceptibility of surgical magnesium alloy in artificial biological fluid containing albumin, J. Mater. Res. 22 (2007) 1806–1814.

[81] F. Witte, N. Hort, C. Vogt, S. Cohen, K.U. Kainer, R. Willumeit, F. Feyerabend, Degradable biomaterials based on magnesium corrosion, Curr. Opin. Solid State Mater. Sci. 12 (2008) 63–72.

[82] D. Zhao, F. Witte, F. Lu, J. Wang, J. Li, L. Qin, Current status on clinical applications of magnesium-based orthopaedic implants: a review from clinical translational perspective, Biomaterials 112 (2017) 287–302.

[83] D. Dziuba, A. Meyer-Lindenberg, J.M. Seitz, H. Waizy, N. Angrisani, J. Reifenrath, Long-term in vivo degradation behaviour and biocompatibility of the magnesium alloy ZEK100 for use as a biodegradable bone implant, Acta Biomater. 9 (2013) 8548–8560.

[84] C. Rössig, N. Angrisani, P. Helmecke, S. Besdo, J.-M. Seitz, B. Welke, N. Fedchenko, H. Kock, J. Reifenrath, In vivo evaluation of a magnesium-based degradable intramedullary nailing system in a sheep model, Acta Biomater. 25 (2015) 369–383.